lubricants

MDPI

Article

The Effect of Kappa Phases on Tribocorrosion Behaviour of Nickel Aluminum Bronze (NAB) and Manganese Aluminum Bronze (MAB)

Carlos Berlanga-Labari [1,*], Adrián Claver [1], María Victoria Biezma-Moraleda [2] and José Fernández-Palacio [3]

[1] Institute for Advanced Materials and Mathematics (INAMAT²), Public University of Navarre, Campus Arrosadía s/n, 31006 Pamplona, Spain; adrian.claver@unavarra.es
[2] Departamento de Ciencia e Ingeniería del Terreno y de los Materiales, Universidad de Cantabria, 39004 Santander, Spain; maria.biezma@unican.es
[3] Centre of Advanced Surface Engineering, AIN, Cordovilla, 31191 Pamplona, Spain; jfpalacio@ain.es
* Correspondence: carlos.berlanga@unavarra.es

Abstract: Nickel aluminum bronze (NAB) and manganese aluminum bronze (MAB) are widely used in propulsion and seawater handling systems in naval platforms due to their attractive combination of mechanical strength, toughness, and very low susceptibility to marine corrosion. Nevertheless, it is well known that they can suffer from selective phase corrosion and erosion–corrosion, primarily caused by cavitation and sand erosion. Both alloys have a multiphase microstructure that governs their mechanical and chemical behavior. The tribocorrosion behavior of cast NAB and MAB alloys was studied in artificial seawater to analyze the effect on microstructure. The microstructure and nanohardness were evaluated and correlated with tribocorrosion test results conducted under two different loads (10 and 40 N) in a unidirectional sliding mode using a 1 M NaCl solution as the electrolyte. A significant increase in the corrosion rate due to the wear effect was observed in both alloys. MAB exhibited a slightly better tribocorrosion performance than NAB, which was attributed to significant differences in the shape, distribution, and size of the intermetallic kappa phases—rich in iron, aluminum, and nickel—within the microstructure. Pitting corrosion was observed in NAB, while selective corrosion of kappa phases occurred in MAB, highlighting the role of the protective layer in the tribocorrosion behavior of both alloys. These findings were supported by post-test solution analysis using ICP-AES and corrosion product characterization by EDX. A synergistic effect between wear and corrosion was confirmed for both alloys, as erosion removes the protective layer, exposing fresh material to continuous friction and favoring a progressive material loss over time. The practical impact of this study lies in improving the control and design of highly alloyed bronze microstructures under in-service corrosion–erosion conditions.

Keywords: NAB; MAB; kappa phases; tribocorrosion; nanohardness

Received: 10 April 2025
Revised: 10 June 2025
Accepted: 13 June 2025
Published: 29 June 2025

Citation: Berlanga-Labari, C.; Claver, A.; Biezma-Moraleda, M.V.; Fernández-Palacio, J. The Effect of Kappa Phases on Tribocorrosion Behaviour of Nickel Aluminum Bronze (NAB) and Manganese Aluminum Bronze (MAB). *Lubricants* **2025**, *13*, 290. https://doi.org/10.3390/lubricants13070290

Copyright: © 2025 by the author. Licensee MDPI, Basel, Switzerland. This article is an open access article distributed under the terms and conditions of the Creative Commons Attribution (CC BY) license (https://creativecommons.org/licenses/by/4.0/).

1. Introduction

Tribocorrosion is defined as the combined degradation of materials through corrosion and wear under sliding contact while immersed in an electrolyte (i.e., electrically conductive solutions) [1], involving synergistic and continuous mechanical–chemical–electrochemical interactions. Many variables influence tribocorrosion-related material damage, which often results in significant material loss due to the complex superposition

of wear, mechanical action, corrosion, and environmental effects—many of which are still under study [2–7]. Numerous industrial activities [8–12] and materials [13–19] are affected by this phenomenon, which has drawn increasing attention in recent years.

Several studies have addressed the corrosion–erosion behavior of different copper alloys, particularly in seawater. Aslan et al. [20] investigated the effect of alloying Cu–Al with Fe, Ni, Mn, and Ge via powder metallurgy to improve resistance against corrosion–erosion, finding enhanced mechanical performance and significant microstructural changes. Wang et al. [21] studied the influence of erosion time, temperature, and flow rate on a copper–nickel alloy tube, observing that erosion–corrosion was controlled by the passive layer formed on the material. This finding corroborates previous studies [22] which attributed the good erosion–corrosion resistance of 90/10 and 70/30 copper–nickel tubes to the formation of a corrosion product film, particularly due to a Ni-enriched layer at the film/substrate interface. Furthermore, the early formation of a protective layer in Cu–Ni 90/10 alloy pipes exposed to seawater and the role of solid microparticles in the fluid were highlighted in a failure case study [23]. Intergranular erosion–corrosion of pure copper has also been reported as a complex phenomenon controlled by flow velocity, which affects both the morphology and chemical composition of the corrosion layer [24].

Highly alloyed bronze materials are widely used due to their excellent surface performance against wear, cavitation, and erosion, as well as their high corrosion resistance resulting from the development of protective layers in various environments [25–27]. In particular, nickel aluminum bronze (NAB) and manganese aluminum bronze (MAB) are selected for naval sector components such as propellers and shafts, where tribocorrosion behavior is critical due to the continuous synergistic effect of erosion and corrosion over the service life.

NAB and MAB alloys exhibit a complex multiphase microstructure, consisting of a copper-rich alpha phase, an aluminum-rich beta phase, and numerous intermetallic secondary phases known as kappa phases [28,29]. These kappa phases show a random distribution and wide variation in shape and size, which depend strongly on the alloy's chemical composition [30], manufacturing process [31–33], and other factors. While the corrosion susceptibility [34–36] and tribocorrosion behavior [37–39] of these alloys have been studied, relatively little attention has been given to the active role of the kappa phases as intermetallic compounds in the tribocorrosion behavior of metallic materials.

Zhang et al. [38] confirmed selective corrosion of the κ_{IV} phase in a NAB alloy at solution pH values below 4.2. After performing tribocorrosion tests in artificial seawater over a pH range from 3.2 to 10.2, they observed selective corrosion of the α-phase, with preferential attack occurring along the boundaries of intermetallic κ_{III} and κ_{IV} precipitates. Song et al. [39] studied NAB, MAB, and manganese brass (MB), concluding that differences in cavitation–corrosion behavior were mainly governed by the pH of the testing solution and the specific electrochemical behavior of each phase. These differences may promote selective corrosion, leading to reduced corrosion–erosion resistance.

Although some studies have addressed the cavitation and erosion behavior of MAB [39,40], no current research has been specifically devoted to its tribocorrosion behavior. In general, it can be concluded that the complexity of the erosion–corrosion phenomenon arises from the influence of both the passive layer formed during service and the alloy microstructure.

In this study, the comparative tribocorrosion behavior of nickel aluminum bronze (NAB—$CuAl_{10}Fe_5Ni_5$) and a manganese aluminum bronze (MAB—$CuAl_{10}Mn_{12}Fe_5$) was investigated in a 1 M NaCl solution simulating seawater. A sliding contact was established with an inert aluminum oxide ball counter-body under loads of 10 N and 40 N. The experiments were conducted using a pin-on-disk system fitted with an electrochemical cell, operating in unidirectional sliding mode. Material loss was assessed from the wear track

using confocal microscopy. Additionally, micro- and nanohardness measurements of the kappa phases were performed to support the tribocorrosion analysis. The objective of the research was to assess the role of multiphase microstructures in tribocorrosion degradation, with special emphasis on the kappa phases.

2. Materials and Methods

Manganese aluminum bronze (MAB, C95700) was provided in the as-cast condition. The main difference in the chemical composition between MAB and nickel aluminum bronze (NAB) lies in the manganese content (MAB: 12.8%, NAB: 1.2%) and the nickel content (NAB: 4.6%, MAB: 2.1%). Metallographic preparation involved grinding with 320-grit SiC paper, followed by polishing with 9 μm and 3 μm diamond suspensions, and a final polishing step using a 0.05 μm alumina suspension. To reveal the microstructure, specimens were etched for 10 s in a ferric chloride solution (5 g $FeCl_3$, 20 mL HCl, and 80 mL distilled water).

Both alloys were microstructurally characterized using optical microscopy, scanning electron microscopy (SEM), and X-ray diffraction (XRD) in Bragg–Brentano configuration, employing a copper source (Cu Kα radiation; λ = 1.5418 Å) and an angular scan rate of 0.02°/s.

To mechanically characterize the kappa intermetallic compounds, nanohardness measurements were performed using a Hysitron TriboIndenter 950 (Bruker Corporation, Billerica, MA, USA). A maximum load of 10 mN was applied with a loading time of 5 s, holding time of 2 s, and unloading time of 5 s. A Berkovich tip with a 200 nm radius was used. Data was analyzed using the Oliver and Pharr method [41]. Indentations were performed on kappa I intermetallic compounds, as the other types were not large enough to be indented. Additionally, Vickers microhardness and macrohardness measurements were carried out on both alloys using loads of 100 gf and 1 kgf, respectively. All indentation tests were performed three times, and results are presented as mean values with standard deviations.

Pin-on-disk tests were conducted in 1 M NaCl solution using a Microtest MT series tribometer (Microtest S.A, Madrid, Spain), with 6 mm alumina balls as counterparts and applied loads of 10 N and 40 N. All electrochemical measurements were carried out at room temperature using an Autolab potentiostat and a conventional three-electrode system (counter electrode: Pt; reference electrode: Ag/AgCl).

The coefficient of friction (COF) and open circuit potential (OCP) were measured simultaneously over 3600 s of sliding. Additionally, polarization curves were recorded during sliding at a scanning rate of 0.1 mV/s.

The procedure to quantify the synergistic effect between corrosion and mechanical wear is explained in Figure 1 and involved the following steps: (a) Total material loss in volume (V_{tot}) was determined by weighing the samples before and after the tests and multiplying the mass difference by the specimen density. (b) Material loss due to tribocorrosion (V_{tr}) was obtained by calculating the wear track volume from cross-sectional profiles obtained by confocal microscopy. (c) Material loss due to corrosion on the unworn surface (V_{corr}) was estimated using the following equation (Equation (1)):

$$V_{corr} = V_{tot} - V_{tr} \quad (1)$$

Additionally, corrosion tests were conducted to estimate material loss due to wear-accelerated corrosion (V_{wac}) on the unworn surface of the non-passivating bronze. For this purpose, samples were kept immersed in seawater throughout the test to quantify corrosion without mechanical loading (V_{pc}), applying the following equation (Equation (2)):

$$V_{wac} = V_{corr} - V_{pc} \quad (2)$$

Both weight loss and volume loss measurements were conducted three times.

Finally, the elemental composition of the test media after tribocorrosion experiments was analyzed using Inductively Coupled Plasma Optical Emission Spectroscopy (ICP-AES).

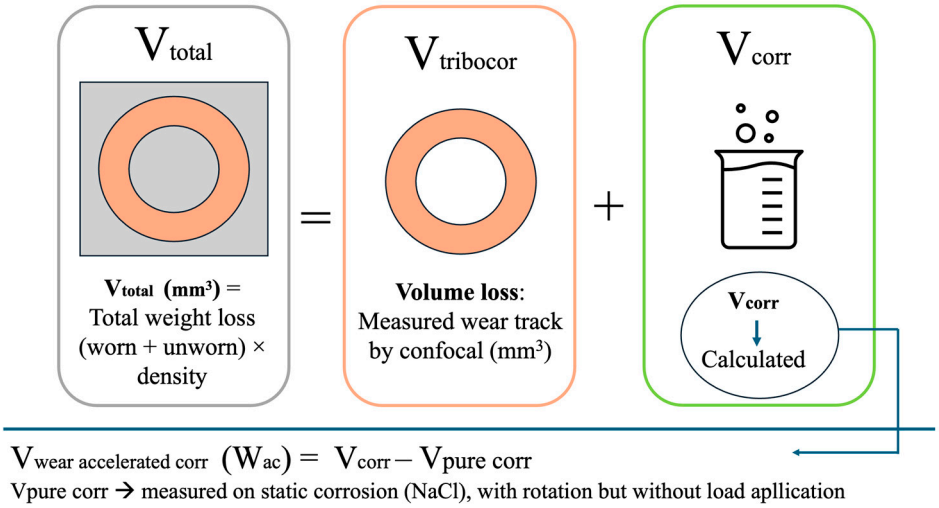

Figure 1. Schematic of the experimental procedure for determining the wear-accelerated corrosion volume, V_{wac}.

3. Results and Discussion

3.1. Chemical and Structural Characterization

The NAB and MAB alloys exhibit a multiphase microstructure, consisting of alpha (α), beta (β), and various intermetallic kappa (κ) phases (Figure 2a,b). Detailed microstructural analysis by SEM (Figure 2c,d) revealed that the majority of the microstructure in NAB is composed of lamellar eutectoid regions of α and κ phases. In contrast, MAB displays large rosette-like kappa phase formations, primarily located within the α phase and/or at α/β interfaces.

(**a**) (**b**)

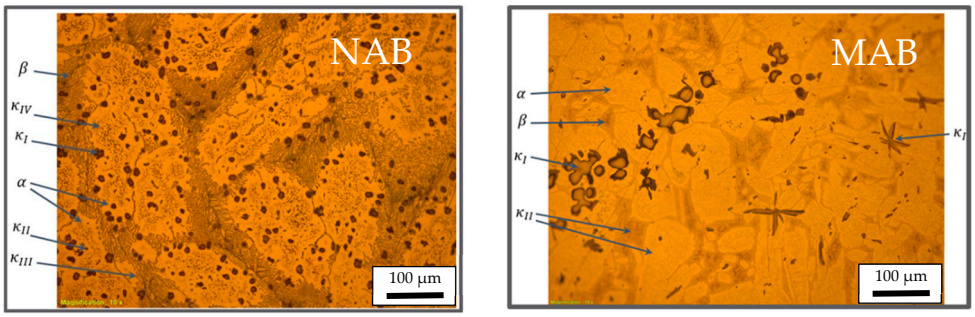

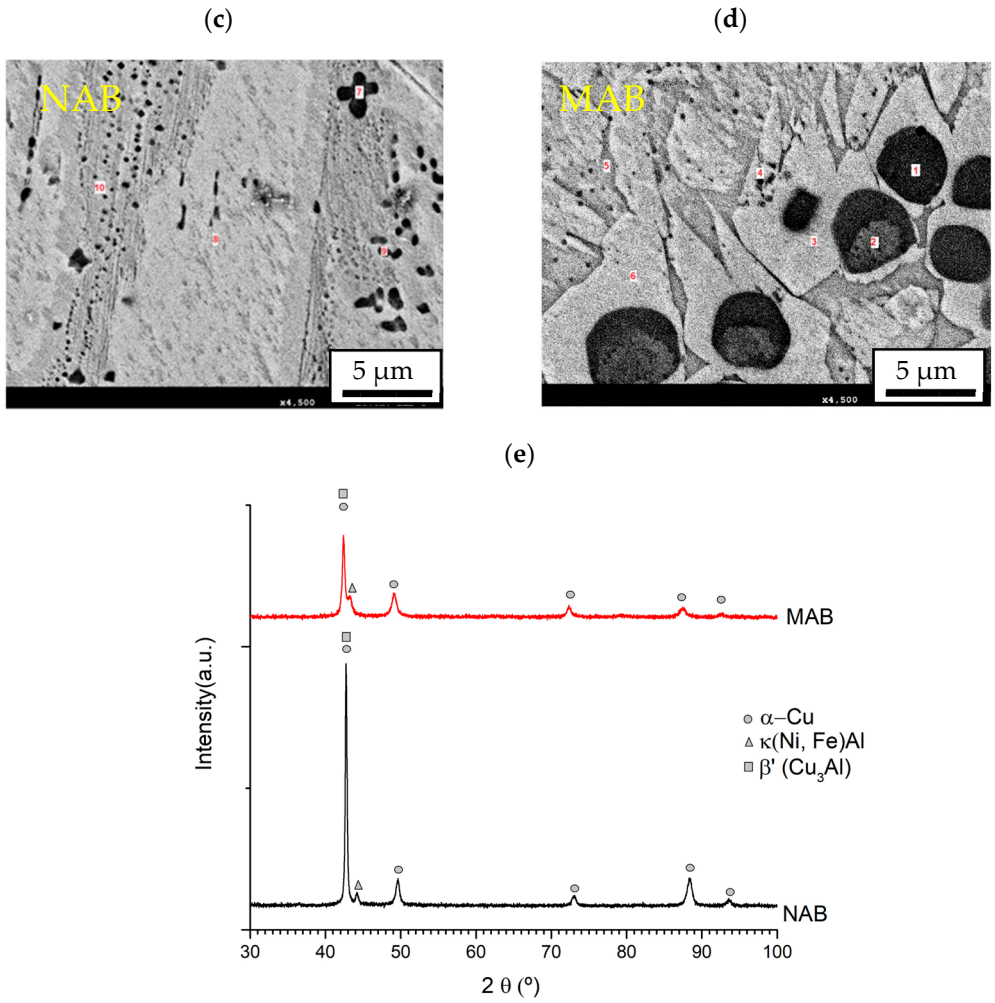

Figure 2. Microstructural characterization of NAB (**left**) and MAB (**right**). Optical Microscopy ×500 (**a**,**b**), SEM Images, ×4500 (**c**,**d**) and XRD diffractograms (**e**).

A careful analysis (Table 1) shows that the percentage of kappa phases is slightly higher in NAB compared to MAB (14.3 ± 1.0% vs. 11.8 ± 0.9%). However, the κ phases in NAB have a smaller average size than those in MAB, measuring 253 ± 34 µm² and 753 ± 65 µm², respectively. The X-ray diffraction results (Figure 2e) confirm the phases identified by light and electron microscopy, revealing the presence of martensitic β′ phase—resulting from the eutectoid reaction—as well as kappa phases rich in Ni, Al, and Fe.

Table 1. Phase quantification of MAB and NAB alloys.

	α Phase (%)	**β Phase (%)**	**Kappa (%)**	**Mean Size Kappa (µm²)**
NAB	52.9	32.3	14.3	253
MAB	57.7	30.4	11.8	753

EDX microanalysis (Table 2) reveals that the kappa intermetallic phases in NAB are richer in Ni compared to those in MAB, which are predominantly rich in Mn.

Table 2. EDX characterization corresponding to the areas marked in Figure 2 (MAB: regions 1–6; NAB: regions 7–10).

	1	**2**	**3**	**4**	**5**	**6**	**7**	**8**	**9**	**10**
Al (%)	6.1	4.8	5.5	7.0	8.4	6.5	11.7	7.7	11.1	10.0

Ni (%)	2.2	2.0	1.7	1.0	3.0	1.7	9.8	6.3	7.8	6.3
Mn (%)	17.8	16.8	12.0	19.9	13.2	11.0	1.7	1.3	1.7	1.3
Fe (%)	62.0	57.6	7.8	14.4	2.5	9.8	52.9	3.7	24.3	7.0
Cu (%)	11.5	18.3	71.0	54.9	70.7	69.0	22.9	84.2	54.5	75.0

3.2. Mechanical Properties

Significant differences were observed between the hardness values of the main phases in both materials. The alpha phase exhibited similar micro- and nanohardness values for both alloys: HV = 130 ± 6 and H = 2.7 ± 0.1 GPa for MAB, and HV = 140 ± 5 and H = 3.1 ± 0.1 GPa for NAB. In contrast, the beta phase showed a noticeable increase in hardness, particularly in MAB (HV = 250 ± 8) compared to NAB (HV = 150 ± 5) (Figure 3).

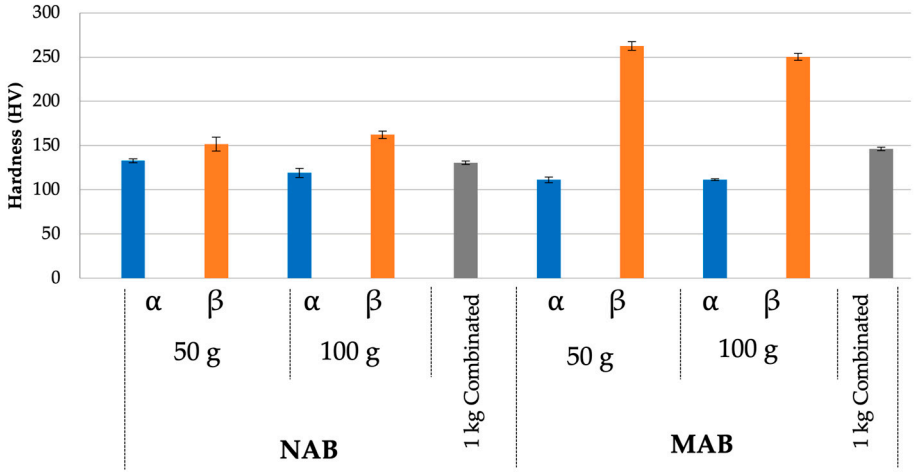

Figure 3. Microhardness and macrohardness results of NAB and MAB alloys.

The microindentations (100 gf) performed on the surfaces of NAB and MAB are shown in Figure 4. These indentations are large enough to affect all microstructural features, including the alpha, beta, and kappa phases.

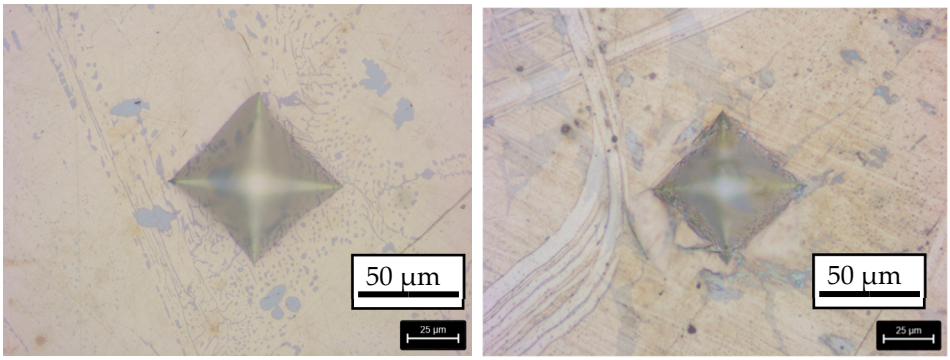

Figure 4. Morphology of Vickers microhardness indentations (100 gf) on the surface of NAB and MAB alloys.

The nanohardness and elastic modulus of the kappa phase are significantly higher in NAB (7.4 ± 0.2 GPa; E = 125 ± 3 GPa) compared to MAB (3.3 ± 0.2 GPa; E = 79 ± 3 GPa). The greater hardness of these intermetallic compounds compensates for the lower hardness of the beta phase, resulting in similar macrohardness values for the two alloys (MAB = 150 ± 6 HV; NAB = 140 ± 5 HV) (Figure 5).

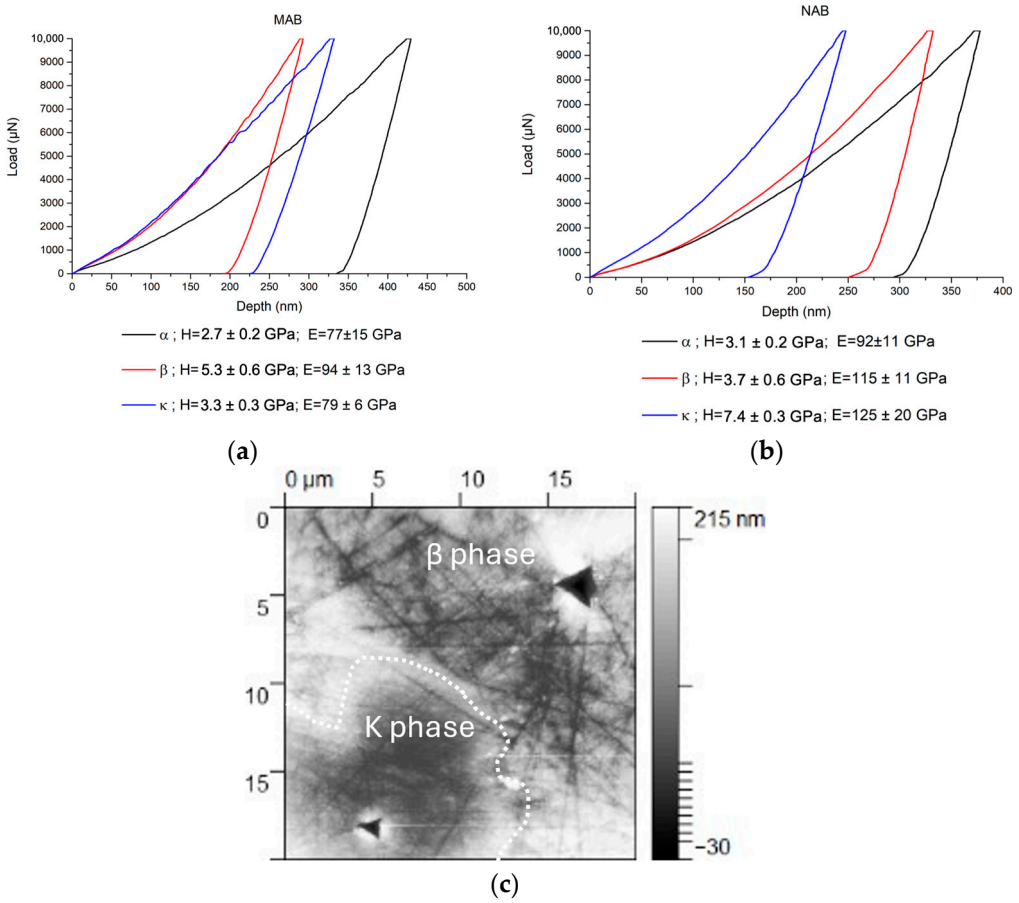

Figure 5. Nanoindentation load–displacement curves (**a**,**b**), and AFM image of an indentation on a kappa phase (**bottom left corner**) compared to a β-phase indent (**top right corner**) in NAB (**c**). The boundary of the kappa phase is indicated by the white dotted line.

The elevated hardness observed in the beta phase of MAB (HV = 250) can be attributed to the extensive formation of kappa intermetallic compounds. In addition, the higher hardness of NAB kappa intermetallics is associated with their distinct chemical and crystallographic nature.

There is a clear influence of microstructure on mechanical properties, particularly related to the size, distribution, shape, and chemical composition of the kappa phases—Ni-rich in NAB and Mn-rich in MAB—as well as the chemistry of the beta phase. The balance of the final mechanical properties reflects an optimal combination of the hardness contributions from each individual phase.

3.3. Corrosion and Tribocorrosion Properties

The corrosion rates under static conditions are low (0.02 mm/y), but a notable increase is observed under applied load, reaching approximately 0.1 mm/y, as shown by the Tafel curve analysis (Figure 6a). Under static conditions, both NAB and MAB form a protective surface layer rich in copper and aluminum, which reduces the corrosion rate. However, during sliding, this protective layer is continuously removed, leading to a significant increase in corrosion rate due to the mechanical wear effect.

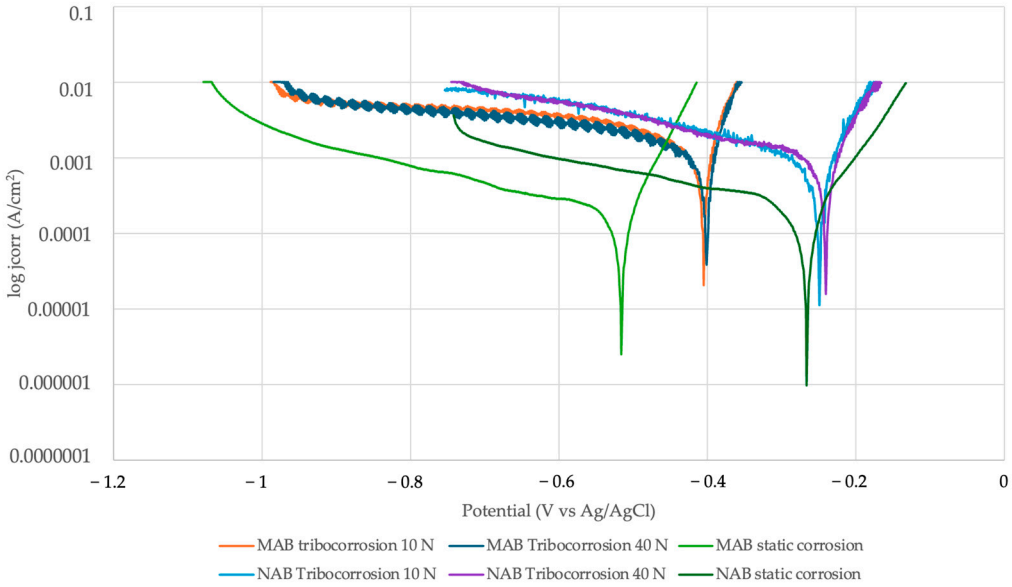

(**a**)

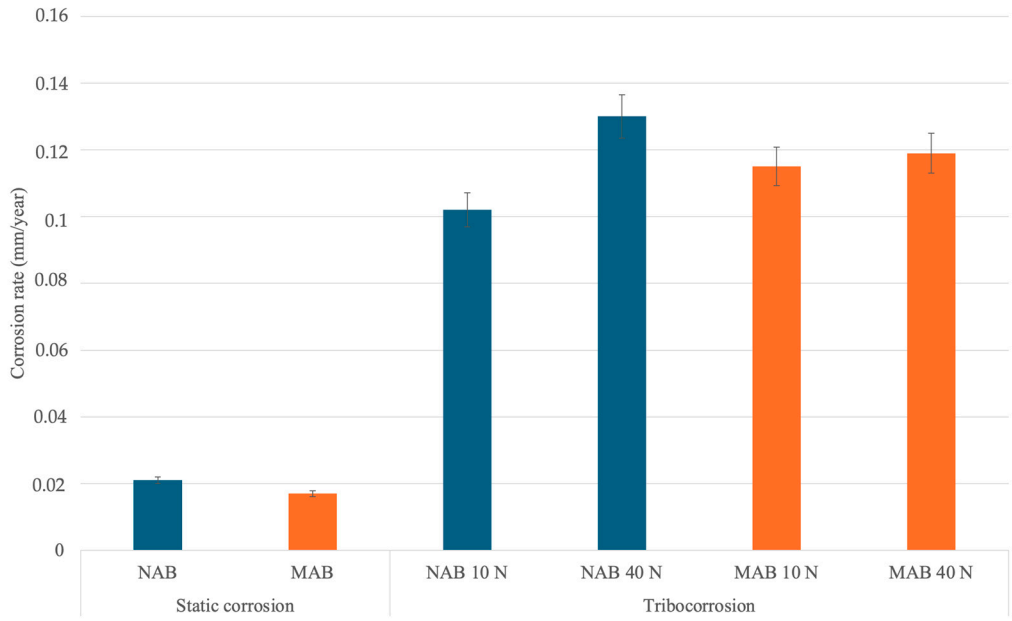

(**b**)

Figure 6. Static and dynamic polarization curves in 1 M NaCl solution (**a**), and corrosion rates (mm/year) under static and dynamic (tribocorrosion) conditions (**b**).

The open circuit potential (OCP) of MAB is more negative (E = −500 mV) than that of NAB (E = −250 mV), indicating a higher tendency towards corrosion. Neither alloy exhibits passivation behavior during anodic polarization. In NAB, anodic metal dissolution is activated by wear, which removes the protective layer and results in a drop in E_{OCP}. In contrast, MAB shows an initial increase in E_{OCP}, likely due to enhanced oxygen transport to the poorly protected and actively corroding surface. This behavior is particularly evident at the lower applied force of 10 N.

The coefficients of friction (COF) for NAB and MAB range from 0.10 to 0.25, except for MAB under a 10 N load, where the COF increases up to 0.35 (Figure 7). During anodic polarization, a greater increase in COF was observed in MAB compared to NAB, which may be attributed to the different nature of the friction–corrosion products generated

during the test, resulting from the interaction between the electrolyte, the material, and mechanical forces.

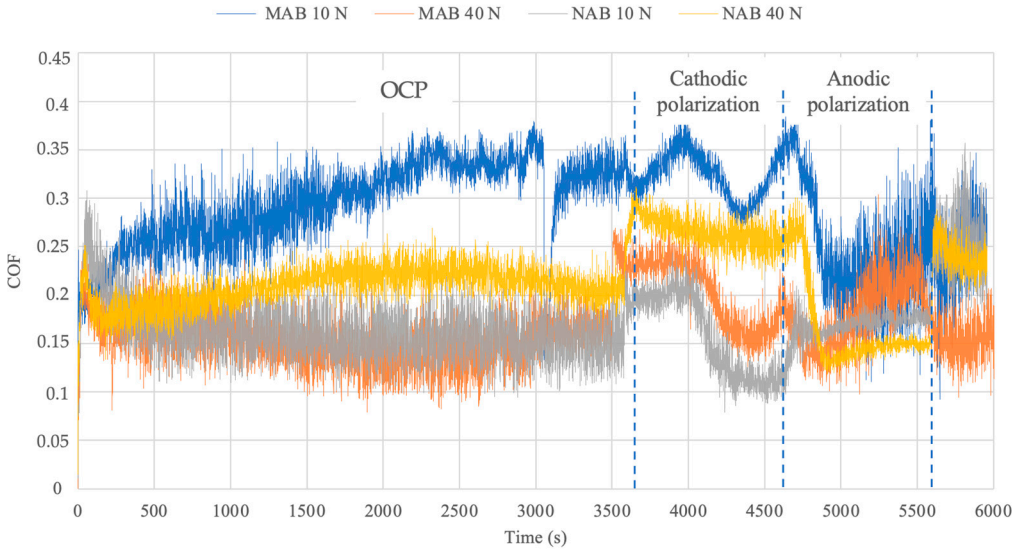

Figure 7. COF vs. time obtained during polarization tests.

Therefore, under the 10 N load, the dominance of a wear-induced corrosion mechanism may be supported by the easy removal of the porous surface layer. This leads to continuous exposure of fresh, unprotected material to the electrolyte, allowing the corrosion process to proceed at a higher rate than it would if the porous layer remained intact.

The volume loss in the wear track is significantly higher in NAB for both applied loads (10 N: NAB k = 5.5 × 10^{-6} mm^3/Nm, MAB k = 2.2 × 10^{-6} mm^3/Nm; 40 N: NAB k = 1.6 × 10^{-5} mm^3/Nm, MAB k = 6.1 × 10^{-6} mm^3/Nm) (Figure 8a), resulting in a higher wear coefficient for the NAB alloy. This may be explained by the different tribocorrosion mechanisms observed. The kappa phases in NAB exhibit less noble behavior than those in MAB due to their higher aluminum content, acting as anodic regions relative to the matrix. Corrosion appeared to be more uniformly distributed in NAB based on the wear track morphology analysis.

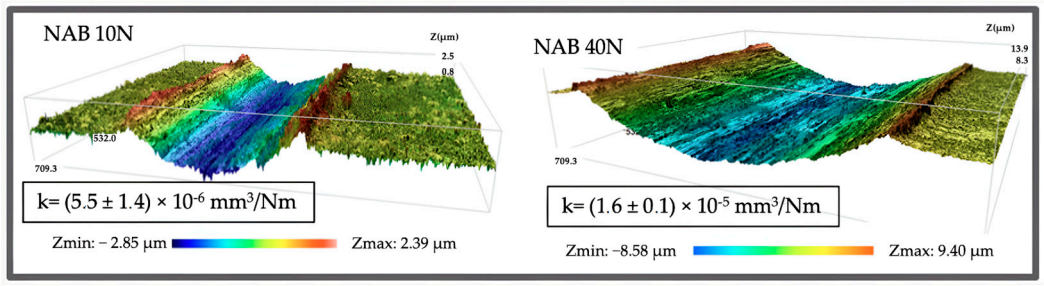

(**a**)

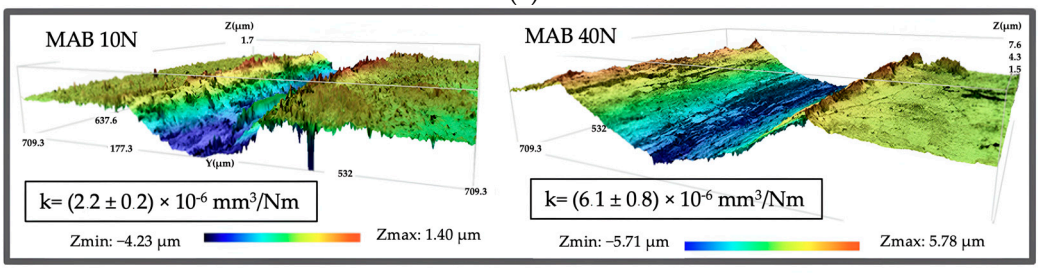

(**b**)

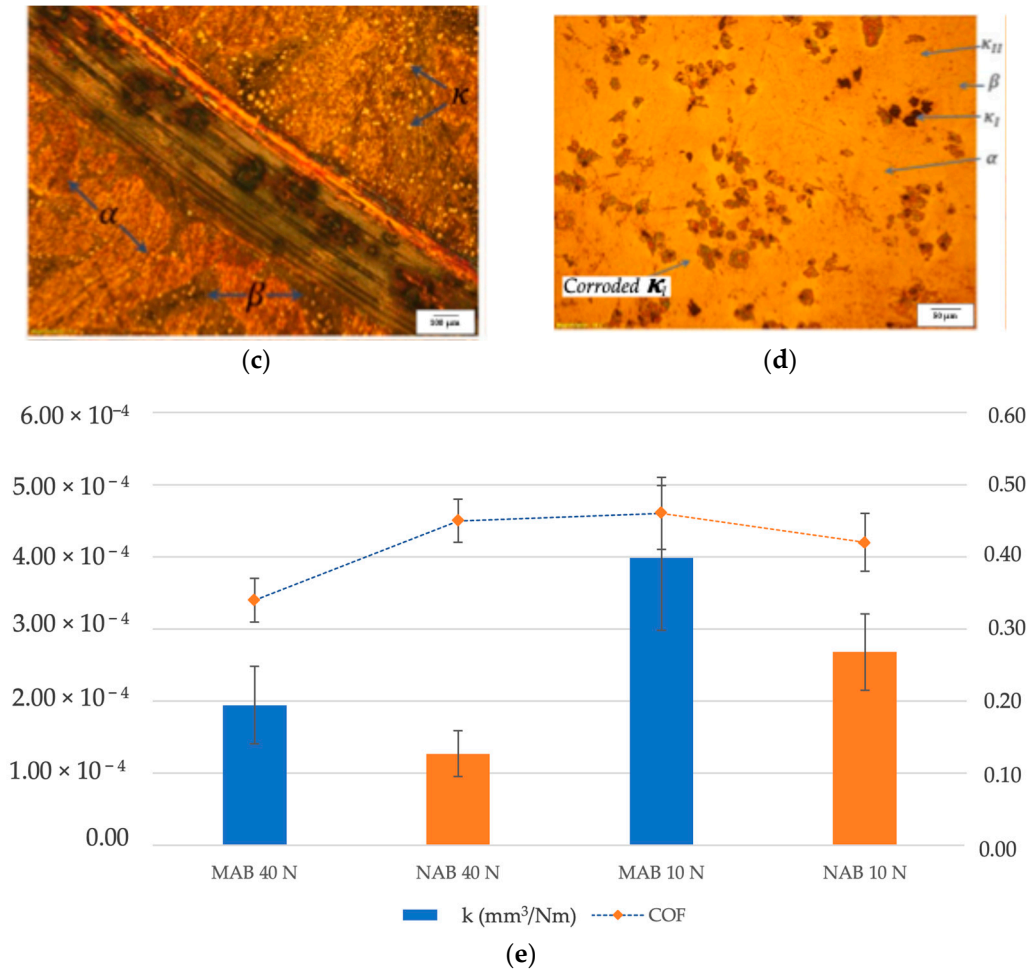

Figure 8. Confocal images of the wear track after the tribocorrosion test (**a**,**b**); optical image of the wear track in NAB at 200× magnification (**c**); optical image of the unworn zone in MAB at 100× magnification (**d**); and wear coefficient and COF results (**e**).

Additionally, extensive plastic deformation was observed in NAB, particularly along the alpha phase and at alpha/beta interfaces. This likely caused the α-phase network in the microstructure to become more irregular and discontinuous under the higher load, accompanied by altered shapes and distribution of kappa phases.

In NAB, the smaller size of the kappa phases likely contributes to higher local current densities and ultimately to a higher corrosion rate, resulting in pitting within the wear track where these phases are located (Figure 8c). Conversely, the larger iron- and manganese-rich rosette-like kappa phases in MAB may promote selective corrosion at the kappa and alpha/kappa interfaces in the unworn zones (Figure 8d).

Most of the material volume loss associated with corrosion is primarily due to a wear-accelerated corrosion mechanism (V_{wac}) with only a minor contribution from so-called pure corrosion (V_{pc}) (Figure 9). These results are consistent with those reported by other authors in previous studies [39,40]. It can be concluded that a synergistic effect exists between wear and corrosion for both alloys studied. Erosion removes the protective layer, leading to continuous friction on the freshly exposed, unprotected surface, thereby facilitating significant material loss over time.

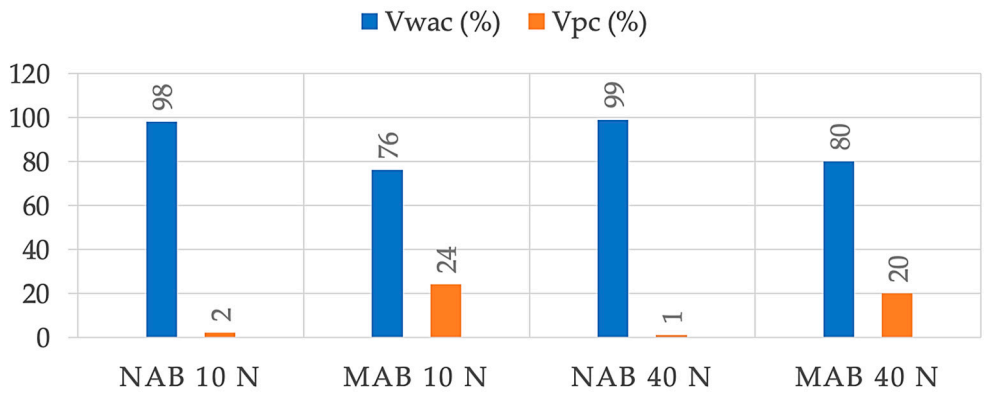

Figure 9. Results of lost volume (%) by V_{wac} (wear accelerated corrosion) and V_{pc} (pure corrosion).

The tribocorrosion test solution was analyzed after each experiment and revealed significant differences, particularly in the concentrations of Cu^{+}, Fe^{2+}, and Mn^{3+} cations (Table 3). The solution from the NAB tests showed a higher concentration of copper and aluminum ions, attributed to the removal of the protective layer during the tribocorrosion process. In contrast, the solution from the MAB tests exhibited a higher concentration of iron and manganese ions compared to the NAB results. The elevated manganese content in the MAB solution is associated with the chemical composition of its intermetallic compounds as well as its beta phase.

Table 3. Elemental ion chemical analysis (ICP-AES) of the electrolyte after tribocorrosion test.

	Cu (mg/L)	Ni (mg/L)	Al (mg/L)	Fe (mg/L)	Mn (mg/L)
NAB	29.66 ± 1.32	0.72 ± 0.05	3.24 ± 0.18	1.36 ± 0.06	0.57 ± 0.02
MAB	1.19 ± 0.06	0.25 ± 0.02	1.71 ± 0.13	13.18 ± 0.45	6.98 ± 0.08

This observation is consistent with findings reported by Wang et al. [42], who noted that large intermetallic compounds in 7075 aluminum alloys tend to detach from the microstructure. Furthermore, these results suggest a balance between the susceptibility of the protective layer to dissolution or erosion and the corrosion of specific kappa phases in both alloys. This behavior appears to be linked to the chemical composition and morphology of the kappa phases. In MAB, kappa phases predominantly appear as rosette-like structures, which exhibit high interfacial energy with the surrounding alpha-phase matrix. In contrast, kappa phases in NAB range from globular shapes—rich in Fe and Al—to lamellar or elongated forms, rich in Ni and Al (Figure 2e).

4. Conclusions

In this study, the influence of kappa intermetallic phases in NAB and MAB alloys on their tribocorrosion behavior in a marine environment was analyzed. It was found that the percentage, size, chemical composition, and morphology of the kappa intermetallic phases differ between the two alloys. Specifically, the NAB alloy contains a higher proportion of intermetallic compounds (14.3%) compared to the MAB alloy (11.8%), although with a significantly smaller average size (253 ± 34 μm² vs. 753 ± 65 μm²). Additionally, nanohardness measurements revealed that the kappa phases in NAB exhibit significantly higher values than those in MAB (7.4 ± 0.2 GPa vs. 3.3 ± 0.2 GPa).

A synergistic mechanical and electrochemical effect, known as wear-accelerated corrosion, was observed in both alloys when tested under loads of 10 N and 40 N in a simulated marine environment. The MAB alloy exhibited slightly better tribocorrosion performance than NAB, which can be attributed to differences in the chemical nature and size

of the kappa intermetallic phases, as well as the composition of the protective surface layers.

The corrosion–friction synergistic mechanism observed in these highly alloyed bronzes can be described as follows: mechanical wear removes the protective oxide layers in both alloys, exposing fresh metal surfaces that are susceptible to different corrosion mechanisms depending on the alloy. In the case of NAB (nickel aluminum bronze), this manifests primarily as pitting corrosion. In contrast, MAB (manganese aluminum bronze) exhibits more selective corrosion, particularly at the kappa/alpha phase interfaces.

To further understand this complex phenomenon, it is recommended to study additional environmental factors that may influence the tribocorrosion behavior of NAB and MAB alloys, such as temperature, the presence of biofilms, and mechanical stress. This would help to more accurately simulate the real-world performance of these alloys and define appropriate directions for future research.

Author Contributions: Conceptualization, C.B.-L. and M.V.B.-M.; methodology, C.B.-L., M.V.B.-M., A.C. and J.F.-P.; validation, C.B.-L., M.V.B.-M., A.C. and J.F.-P.; formal analysis, C.B.-L., A.C. and J.F.-P.; investigation, C.B.-L., M.V.B.-M., A.C. and J.F.-P.; resources, C.B.-L., M.V.B.-M. and J.F.-P.; data curation, C.B.-L. and A.C.; writing—original draft preparation, C.B.-L., M.V.B.-M., A.C. and J.F.-P.; writing—review and editing, C.B.-L. and A.C.; supervision, C.B.-L.; project administration, C.B.-L. All authors have read and agreed to the published version of the manuscript.

Funding: This research received no external funding.

Data Availability Statement: The original contributions presented in this study are included in the article. Further inquiries can be directed to the corresponding author(s).

Acknowledgments: The authors would like to thank JC Navalips, Cantabria, Spain, for supplying the materials used in this study.

Conflicts of Interest: The authors declare no conflicts of interest.

Abbreviations

The following abbreviations are used in this manuscript:

MAB	Manganese-Aluminum Bronze
NAB	Nickel-Aluminum Bronze
SEM	Scanning Electron Microscopy (SEM)
XRD	X-ray diffraction (COF)
COF	coefficient Of Friction
OCP	Open Circuit Potential

References

1. Ponthiaux, P.; Wenger, F.; Drees, D.; Celis, J.P. Electrochemical techniques for studying tribocorrosion processes. *Wear* **2004**, *256*, 459–468. https://doi.org/10.1016/S0043-1648(03)00556-8.
2. Stack, M.M. Mapping tribo-corrosion processes in dry and in aqueous conditions: Some new directions for the new millennium. *Tribol. Int.* **2002**, *35*, 681–689. https://doi.org/10.1016/S0301-679X(02)00059-2.
3. De Stefano, M.; Ruggiero, A. Tribocorrosion of couplings in seawater environment: An investigation on the positive-negative role of synergy. *Tribol. Int.* **2024**, *200*, 110143. https://doi.org/10.1016/j.triboint.2024.110143.
4. Munoz, A.I.; Espallargas, N.; Mischler, S. *Tribocorrosion*; Springer International Publishing: Cham, Switzerland, 2020; pp. 93–94.
5. Mischler, S.; Debaud, S.; Landolt, D. Wear-accelerated corrosion of passive metals in tribocorrosion systems. *J. Electrochem. Soc.* **1998**, *145*, 750.
6. Wood, R.J. Marine wear and tribocorrosion. *Wear* **2017**, *376*, 893–910.
7. Anaee, R.A.M.; Abdulmajeed, M.H. Tribocorrosion. In *Advances in Tribology*; Darji, P.H., Ed.; IntechOpen: London, UK, 2016; pp. 89–110. https://doi.org/10.5772/63657.

8. Pei, W.; Pei, X.; Xie, Z.; Wang, J. Research progress of marine anti-corrosion and wear-resistant coating. *Tribol. Int.* **2024**, *198*,109864. https://doi.org/10.1016/j.triboint.2024.109864.
9. Min, J.; Wang, X.-Z.; Wang, Y.; Bai, Y.; Sabola, S.A.; Gong, W.; Wang, L.; Li, J.; Li, Z. Tribocorrosion in nitric acid of Zr alloy, Ti alloy, and 310 SS used for reprocessing of spent nuclear fuel. *Tribol. Int*. **2024**, *201*, 110184. https://doi.org/10.1016/j.triboint.2024.110184.
10. He, X.; Kumara, C.; Sulejmanovic, D.; Keiser, J.R.; Gallego, N.; Qu, J. Tribocorrosion of stainless steel sliding against graphite in FLiNaK molten salt. *Wear* **2023**, *522*, 204706. https://doi.org/10.1016/j.wear.2023.204706.
11. Okoani, A.O.; Nand, A.; Jiang, C.P.; Ramezani, M. Investigating the Tribocorrosion Behaviour of NiTiNOL60 Alloy in Engineering and Biomedical Applications—An Overview. *Metals* **2004**, *14*, 1334. https://doi.org/10.3390/met14121334.
12. Bueno, A.H.S.; Solis, J.; Zhao, H.; Wang, C.; Simoes, T.A.; Bryant, M.; Neville, A. Tribocorrosion evaluation of hydrogenated and silicon DLC coatings on carbon steel for use in valves, pistons and pumps in oil and gas industry. *Wear* **2018**, *394–395*, 60–70. https://doi.org/10.1016/j.wear.2017.09.026.
13. Li, Z.; Yu, H.; Sun, D. The tribocorrosion mechanism of aluminum alloy 7075-T6 in the deep ocean. *Corros. Sci*. **2021**, *183*, 109306. https://doi.org/10.1016/j.corsci.2021.109306.
14. Silva, R.C.C.; Nogueira, R.P.; Bastos, I.N. Tribocorrosion of UNS S32750 in chloride medium: Effect of the load level. *Electrochim. Acta* **2011**, *56*, 8839–8845. https://doi.org/10.1016/j.electacta.2011.07.077.
15. Sousa, L.; Basilio, L.; Alves, A.C.; Toptan, F. Tribocorrosion-resistant biofunctionalized Ti-Al_2O_3 composites. *Surf. Coat. Technol*. **2021**, *420*, 127329. https://doi.org/10.1016/j.surfcoat.2021.127329.
16. Mégret, A.; Prince, L.; Olivier, M.G.; Vitry, V. Tribo-and tribocorrosion properties of magnesium AZ31 alloy. *Coatings* **2023**, *13*, 448. https://doi.org/10.3390/coatings13020448.
17. Akinribide, O.J.; Akinwamide, S.O.; Obadele, B.A.; Ogundare, O.D.; Ayeleru, O.O.; Olubambi, P.A. Tribological behaviour of ductile and austempered grey cast iron under dry environment. *Mater. Today Proc.* **2021**, *38*, 1174–1182. https://doi.org/10.1016/j.matpr.2020.07.473.
18. Possoli, F.A.A.; Souza, A.P.N.; Bernardelli, E.A.; Borges, P.C. Tribocorrosion assessment of low-temperature plasma nitrided super duplex stainless steel. *Surf. Coat. Technol*. **2024**, *479*, 130572. https://doi.org/10.1016/j.surfcoat.2024.130572.
19. Bidiville, A.; Favero, M.; Stadelmann, P.; Mischler, S. Effect of surface chemistry on the mechanical response of metals in sliding tribocorrosion systems. *Wear* **2007**, *263*, 207–217. https://doi.org/10.1016/j.wear.2007.01.066.
20. Aslan, N.S.; Rajih, A.K.; Haleem, A.H. Effect of Alloying Elements on the Erosion–Corrosion Behaviour of Cu-Based Alloys. *IOP Conf. Ser. Mater. Sci. Eng.* **2020**, *987*, 012018.
21. Wang, K.; Tian, X.; Liu, X.; Wang, G.; Deng, J. Study on the erosion-corrosion behavior of copper-nickel alloys in high temperature and high humidity marine environment. *J. Phys. Conf. Ser.* **2025**, *2951*, 012103.
22. Wu, L.; Xu, Y.; Ma, A.; Zhang, L.; Zheng, Y. Influence of pre-immersion aeration conditions on corrosion product films and erosion-corrosion resistance of 90/10 and 70/30 copper-nickel tubes in 1 wt% NaCl solution. *Corros. Sci*. **2024**, *228*, 111817. https://doi.org/10.1016/j.corsci.2024.111817.
23. Lin, S.; Li, D.; Zhou, Q.; Chu, M.; Sun, Y.; Liu, M.; Zheng, K.; Qiao, S.; Zhao, L.; Zhao, L.; et al. Study on corrosion perforation behavior of copper nickel alloy pipe during service in marine environment. *Eng. Fail. Anal*. **2023**, *153*, 107628. https://doi.org/10.1016/j.engfailanal.2023.107628.
24. Wu, L.; Ma, A.; Zhang, L.; Zheng, Y. Intergranular erosion corrosion of pure copper tube in flowing NaCl solution. *Corros. Sci*. **2022**, *201*, 110304. https://doi.org/10.1016/j.corsci.2022.110304.
25. Kosec, T.; Ćurković, H.O.; Legat, A. Investigation of the corrosion protection of chemically and electrochemically formed patinas on recent bronze. *Electrochim. Acta* **2010**, *56*, 722–731. https://doi.org/10.1016/j.electacta.2010.09.093
26. Chiavari, C.; Rahmouni, K.; Takenouti, H.; Joiret, S.; Vermaut, P.; Robbiola, L. Composition and electrochemical properties of natural patinas of outdoor bronze monuments. *Electrochim. Acta* **2007**, *52*, 7760–7769. https://doi.org/10.1016/j.electacta.2006.12.053.
27. Zahner, L.W. *Copper, Brass, and Bronze Surfaces: A Guide to Alloys, Finishes, Fabrication and Maintenance in Architecture and Art*; John Wiley and Sons: Hoboken, NJ, USA, 2020.
28. Culpan, E.A.; Rose, G.R.F. Microstructural characterization of cast nickel aluminium bronze. *J. Mater. Sci.* **1978**, *13*, 1647–1657. https://doi.org/10.1007/bf00548728.
29. Lloyd, D.; Lorimer, G.W.; Ridley, N. Characterization of phases in a nickel-aluminium bronze. *Metals Technol*. **1980**, *7*, 114–119. https://doi.org/10.1179/030716980803286577.

30. Poojary, S.; Marakini, V.; Rao, R.N.; Vijayan, V. Enhancing microstructure and mechanical properties of nickel aluminium bronze alloy through tin addition. *Sci. Rep*. **2023**, *13*, 16907.
31. Küçükömeroğlu, T.; Şentürk, E.; Kara, L.; İpekoğlu, G.; Çam, G. Microstructural and mechanical properties of friction stir welded nickel-aluminum bronze (NAB) alloy. *J. Mater. Eng. Perform*. **2016**, *25*, 320–326. https://doi.org/10.1007/s11665-015-1838-x.
32. Orzolek, S.M.; Semple, J.K.; Fisher, C.R. Influence of processing on the microstructure of nickel aluminum bronze (NAB). *Addit. Manuf.* **2022**, *56*, 102859. https://doi.org/10.1016/j.addma.2022.102859.
33. Luca, R.; Nascimento, P.H.T.; Santos, V.T.; Silva, M.R.; Lobo, F.G.; Teram, R.; Nascimento, M.S.; Couto, A.A.; Filho, A.M.; dos Santos, G.A. Correlation of Solidification Thermal Variables with Microstructure and Hardness in CuMn11Al8Fe3Ni3 Manganese–Aluminum–Bronze Alloy. *Materials* **2025**, *18*, 234. https://doi.org/10.3390/ma18020234.
34. Böhm, J.; Linhardt, P.; Strobl, S.; Haubner, R.; Biezma, M.V. Microstructure of a heat treated nickel-aluminum bronze and its corrosion behavior in simulated fresh and sea water. *Mater. Perform. Charact*. **2016**, *5, 689-700*, https://doi.org/10.1520/MPC20160029.
35. Haubner, R.; Strobl, S.; Ball, G.; Linhardt, P.; Biezma, M.V. Effects of heat treatment on the microstructure and corrosion behavior of manganese aluminum bronzes. *Pract. Metallogr.* **2024**, *61*, 769–782. https://doi.org/10.1515/pm-2024-0068.
36. Wharton, J.A.; Barik, R.C.; Kear, G.; Wood, R.J.K.; Stokes, K.R.; Walsh, F.C. The corrosion of nickel–aluminium bronze in seawater. *Corros. Sci*. **2005**, *47*, 3336-3367. https://doi.org/10.1016/j.corsci.2005.05.053.
37. Huttunen-Saarivirta, E.; Isotahdon, E.; Metsäjoki, J.; Salminen, T.; Carpén, L.; Ronkainen, H. Tribocorrosion behaviour of aluminium bronze in 3.5 wt.% NaCl solution. *Corros. Sci.* **2018**, *144*, 207–223. https://doi.org/10.1016/j.corsci.2018.08.058.
38. Zhang, B.B.; Wang, J.Z.; Yuan, J.Y.; Yan, F.Y. Tribocorrosion behavior of nickel aluminum bronze in seawater: Identification of corrosion-wear components and effect of pH. *Mater. Corros.* **2018**, *69*, 106–114. https://doi.org/10.1002/maco.201709648.
39. Song, Q.N.; Li, H.L.; Nan, X.U.; Jiang, Z.Y.; Zhang, G.Y.; Bao, Y.F.; Jiang, Y.-F.; Zhao, L.-J.; Ji, C.-C.; Zhao, J.-H.; et al. Selective phase corrosion and cavitation erosion behaviors of various copper alloys in 3.5% NaCl solutions with different pH values. *Trans. Nonferrous Met. Soc. China* **2023**, *33*, 3039–3053. https://doi.org/10.1016/S1003-6326(23)66316-2.
40. Tini, S.C.; Zeren, A.; Avcu, Y.Y.; Abakay, E.; Guney, M.; Avcu, E. Cavitation erosion behaviour of MAB-CU4 alloy: Influences of cavitation number, attack angle, time, and stand-off distance. *Mater. Res. Express* **2024**, *11*, 116506. https://doi.org/10.1088/2053-1591/ad8d34.
41. Oliver, W.C.; Pharr, G.M. An Improved technique for determining hardness and Elastic Modulus using load and displacement sensing indentation experiments. *J. Mater. Res*. **1992**, *7*, 1564–1583. https://doi.org/10.1557/JMR.1992.1564.
42. Yan, Q.; Zhang, H.; Man, C.; Pang, K.; Wang, X.; Cui, Z.; Cui, H. The Effect of Intermetallic Compounds on Corrosion and Tribocorrosion Behavior of 7075 Aluminum Alloy. *J. Mater. Eng. Perform.* **2024**, *33*, 11494–11509. https://doi.org/10.1007/s11665-023-08771-y.

Disclaimer/Publisher's Note: The statements, opinions and data contained in all publications are solely those of the individual author(s) and contributor(s) and not of MDPI and/or the editor(s). MDPI and/or the editor(s) disclaim responsibility for any injury to people or property resulting from any ideas, methods, instructions or products referred to in the content.